Improved Kinetics and Stabilities in Mg-Substituted $LiMnPO_4$

Guoying Chen,[*a] Alpesh K. Shukla,[a] Xiangyun Song[a] and Thomas J. Richardson[a]

Abstract

$LiMg_xMn_{1-x}PO_4$ (x = 0, 0.1, 0.2, 0.3, 0.4 and 0.5) crystals were prepared hydrothermally. The presence of Mg^{2+} was found to improve the kinetics, utilization, and physical stability of the crystals during chemical and electrochemical delithiation, as well as the thermal stability of the delithiated phase. The best performance was found in the sample with 20% substitution. The positive effect of Mg^{2+} was attributed to the reduced volume mismatch between the lithiated and delithiated phases, and to more favorable particle morphologies. Mg^{2+} dilutes the concentration of Jahn-Teller active ion, Mn^{3+}, and reduces local strains between the phases, and thereby increases the structural stability of the crystals. The result is a reduction in fracturing and decrepitation, which translates to improved electrochemical performance. Although the thermal stability improved with increasing Mg substitution, the heat evolved during reaction with electrolyte remains proportional to the Mn content and therefore to the theoretical capacity.

[a] *Environmental Energy Technologies Division, Lawrence Berkeley National Laboratory, Berkeley, California 94720 USA*

1. Introduction

The strong P-O covalent bond in the orthorhombic lattice has made the olivine-type Li*M*PO_4 (*M* = Fe, Mn, Co, Ni) compounds attractive cathode materials for lithium-ion batteries. [1] After years of development, $LiFePO_4$ is now mass-produced for commercial high power batteries. Despite its nearly ideal potential of 4.1 V vs. Li/Li^+, lithium manganese phosphate has been found to be an inferior cathode material compared to $LiFePO_4$. [2,3] The much slower kinetics during Li extraction and insertion are directly related to fundamental differences, including lower electronic and ionic conductivities in $LiMnPO_4$, the Jahn-Teller effect in Mn^{3+}, larger interface strain due to the larger volume change between $LiMnPO_4$ and $MnPO_4$, and the metastable nature of the delithiated phase. Recent experimental [4] and theoretical studies [5] have shown that, unlike $FePO_4$, delithiated $LiMnPO_4$ is thermally unstable, evolving oxygen beginning at 150 ^oC and releasing a large amount of heat (884 J/g) upon reaction with a lithium-ion electrolyte such as 1M $LiPF_6$ in 1:1 ethylene carbonate (EC)/propylene carbonate (PC).

Most efforts to improve the kinetic performance of $LiMnPO_4$ have focused on particle size reduction, [6-10] which increases the rate capability and utilization, but inevitably decreases the volumetric energy density of the electrode. Larger surface area also enhances the reactivity of the material toward the electrolyte, thereby raising safety and lifetime concerns. We have previously studied substitution of various divalent cations (Mg, Ni, Cu and Zn) on the M-site of $LiMnPO_4$,[11] a technique that has been shown to be effective in improving the performance of $LiFePO_4$.[12,13] Among these, significant kinetic improvement was achieved with Mg substitution. Here we compare

the synthesis, properties and performance of a series of lithium manganese phosphates with a range of Mg content.

2. Experimental

$LiMnPO_4$ crystals were synthesized using the hydrothermal method described previously. [14] $MnSO_4.H_2O$ (Mallinckrodt, Inc) or $Mn(NO_3)_2.4H_2O$ (Aldrich) was mixed with an equimolar amount of H_3PO_4 (85%, J. T. Baker) in deionized and deoxygenated water to give the desired Mn concentration. A 1.5 M LiOH (Spectrum) solution was added slowly with stirring to give Mn:P:Li equal to 1:1:3. Substantial precipitation occurred during this step. After stirring under helium for another 5 min, the reaction mixture was transferred to a 125 ml Teflon-lined reactor, which was tightly sealed after purging with helium, then held at 220 ^oC for 5 h. On cooling to room temperature, the off-white precipitate was filtered, thoroughly washed with deionized water, and dried in a vacuum oven at 60 ^oC for 24 h. The Mg-substituted $LiMnPO_4$ samples were prepared using the same procedure, except that a mixture of $MnSO_4.H_2O$ and $Mg(NO_3)_2.6H_2O$ (>99%, EM Science) with desired Mn/Mg ratio was dissolved in water before adding the H_3PO_4 and LiOH solutions.

Chemical delithiation was achieved by stirring the phosphate samples in aliquots of a 0.1 M solution of nitronium tetrafluoroborate (NO_2BF_4, 95+%, Aldrich) in acetonitrile. The reactions were carried out at room temperature in an argon-filled glovebox with O_2 < 1 ppm and H_2O < 2 ppm. Delithiated samples for *ex-situ* X-ray diffraction (XRD) measurements were heated to 400 ^oC at a rate of 5 ^oC/min and then held at 400 ^oC for 2 h in a tube furnace purged with flowing N_2.

XRD patterns were acquired using a Panalytical Xpert Pro diffractometer equipped with monochromatized Cu Kα radiation. The scan rate was 0.0025°/s in 0.01° steps. Lattice parameters and phase ratios in the oxidized samples were determined by full pattern refinement using Riqas software (Materials Data, Inc.). Differential scanning calorimetry (DSC) was performed using a DSC 7 instrument (Perkin-Elmer). The samples were loaded into hermetically sealed 30 μl stainless steel capsules in the glovebox and then tested from 30 to 400 ^{o}C at a 10 ^{o}C/min heating rate. The gold-gasketted capsules can withstand an internal pressure up to 150 atmospheres, which suppresses the volatilization of solvent and ensures no weight loss during the experiment. The sample size for the solid was typically 5 mg, and the solid to electrolyte ratio was fixed at 2:1 (w/w) to ensure the presence of excess electrolyte during the experiment. Scanning electron microscopy (SEM) images were collected using a Hitachi S-4300 SE/N microscope at 20 kV accelerating voltage. Transmission electron microscopy (TEM) experiments were carried out at the National Center for Electron Microscopy (NCEM) at LBNL, using a Philips CM200 field emission microscope and a JEOL 200CX electron microscope operating at 200 kV. Samples for TEM were gently ground under ethanol, and the resulting dispersion was transferred to a holey carbon film fixed on a 3 mm copper grid. The images were slightly underfocused to reveal the internal structure of the crystals. Electron diffraction patterns were collected using the selected area electron diffraction (SAED) technique. Fourier transform infrared spectroscopy (FTIR) measurements were performed on KBr pellets using a Nicolet 6700 spectrometer in transmission mode with a spectral resolution of 4 cm^{-1}.

For electrode fabrication, fresh phosphate crystals were ball milled with 20 wt% acetylene carbon black. Composite electrodes were prepared by mixing 80 wt% of this mixture, 10 wt% of Kynar 2801 poly(vinylidene fluoride) (PVdF) binder (Elf Atochem North America, Inc.), 5 wt% SFG-6 synthetic flake graphite (Timcal Ltd., Graphites and Technologies), and 5 wt% compressed acetylene black in *N*-methyl methyl-pyrrolidone (NMP) solution. The slurry was spread onto carbon-coated aluminum foil current collectors and dried overnight in air and then in a 120 ^{o}C vacuum oven for 10 h.

Measurements using the potentiostatic intermittent titration technique (PITT) were carried out using a Solartron 1286 potentiostat/galvanostat in a single-compartment three-electrode cell with Li foil counter and reference electrodes. After measuring a stable open circuit voltage (OCV), the potential was increased in increments of 10 mV while the current response and the capacity accumulated during the potential step were recorded. When the current reached 4 $\mu A/cm^2$ (~C/150), the potential was stepped to the next level, and this procedure was repeated up to 4.4 V. Discharging of the electrodes was carried out in the same manner.

Unless otherwise specified, the electrolyte used for the experiments was 1.0 M $LiPF_6$ in a 1:1 mixture of EC and PC (EM Industries, Inc.). All the electrochemical tests were carried out at room temperature in an argon-filled glove box.

3. Results and Discussion

3.1 Synthesis and Characterization

Phase pure $LiMg_xMn_{1-x}PO_4$ crystals (x=0, 0.1, 0.2, 0.3, 0.4 and 0.5) were synthesized by the hydrothermal method. All samples maintained the original olivine

structure, as shown in the XRD patterns in Fig. 1a. The lattice parameters derived from full pattern refinement of the XRD data (Fig. 1b) exhibited a smooth linear decrease in *a*, *b*, *c* and *V* with increasing Mg content, consistent with the formation of solid solutions of the end members, $LiMnPO_4$ and $LiMgPO_4$, as previously reported by Chen et al. [15,16]

FTIR absorption spectra of the unsubstituted and substituted samples are compared in Fig. 2. In the olivine phosphates, the bands between 1000 and 1150 cm^{-1} are attributed to the symmetric and antisymmetric stretching vibrations of the $PO4^{3-}$ anion, while those between 550 and 650 cm^{-1} arise from bending vibrations of the anion and lattice modes. [17] With increasing Mg content, the low frequency bands were largely unaffected, while the higher frequency bands shifted continuously toward higher energy, consistent with an increase in the P-O bond strength due to the decrease in the M-O bond covalency. [18]

We have shown previously that the choice of precursors and the pH of the solution before the hydrothermal treatment had a large impact on the morphology and performance of the prepared $LiMnPO_4$ samples. [19] When $Mn(NO_3)_2$ was used as the Mn source, the unsubstituted $LiMnPO_4$ was obtained as smaller, more discrete crystals as compared with the large aggregates prepared using $MnSO_4$. The small particles also had better kinetic performance. For the synthesis of $LiMg_xMn_{1-x}PO_4$ crystals, $Mg(NO_3)_2$ and $MnSO_4$ were used as precursors to improve the reaction yield. The presence of SO_4^{2-} decreases the solubility and facilitates the precipitation of the final product. The pH of the reaction solutions monotonically decreased from 10.0 to 9.0 as the ratio of $Mg(NO_3)_2$ to $MnSO_4$ increased from 1:9 for $x = 0.1$ to 5:5 for $x = 0.5$. The size and shape of the crystals were found to vary with *x*, most likely due to the change in pH. As shown in the

SEM images (Fig. 3a), the crystals evolved from elongated hexagons for x≤0.2 to more regular hexagonal plates for higher amounts of Mg. The dimensions of the crystals (D_c x D_a x D_b) were 0.8 x 0.3 x 0.1 μm, 1.0 x 0.4 x 0.1 μm, 1.0 x 0.2 x 0.1 μm, 1.0 x 0.6 x 0.1 μm, 1.0 x 0.6 x 0.1 μm and 1.2 x 0.8 x 0.1 μm for x=0, 0.1, 0.2, 0.3, 0.4 and 0.5, respectively. The D_c/D_a ratio of the unsubstituted crystals was 3.0, and reached its highest value of 5.0 at x = 0.2. Further substitution decreased the D_c/D_a dimension ratio to 1.5 for x = 0.5 (Fig. 3b). Interestingly, all the crystals had the same *b* dimension thickness of 100 nm.

3.2 Improved kinetics and physical stability

Our previous studies have shown that chemical or electrochemical delithiation of $LiMnPO_4$ results in the formation of a solid solution phase, Li_yMnPO_4, in the vicinity of $MnPO_4$. [17] The residual Li content in the delithiated phase, *y*, was found to depend upon the global extent of delithiation and the crystalline domain size of the delithiated phase. When unsubstituted $LiMnPO_4$ was chemically oxidized by 50 mol% of NO_2BF_4, only 8% of the material was delithiated. The crystalline domain size of this delithiated phase was only 2 nm, in contrast to 45 nm for the lithiated phase in the fresh sample. Both the mole fraction and domain size of the delithiated phase increased with the amount of oxidant present. With 200 mol% of NO_2BF_4, the sample reached 70% oxidation after reaction at room temperature for 24 h. Full delithiation to Li_yMnPO_4 was achieved by prolonging the reaction to 72 hr, which also increased the domain size of the delithiated phase to 10 nm. The results suggest that the extent of chemical delithiation is not limited by material utilization. The conversion rate during the reaction, which is defined as the ratio between

the delithiated and the lithiated phases, therefore, can be used as a measure for the kinetic performance of the phosphates.

Compared with the unsubstituted material, all of the Mg-substituted $LiMnPO_4$ crystals showed improved kinetics, as suggested by the increased conversion rate. Fig. 4a shows the XRD patterns of the phosphates treated with 50 mol% of the oxidant. Under the same conditions, the sample with $x = 0.2$ had both the highest delithiated phase content (30 %) and the largest delithiated phase domain size (15 nm). The samples containing more Mg had a nearly constant conversion rate of 20%, but the domain sizes were substantially lower (Fig. 4b).

Table 1 summarizes the lattice parameters of the two phases present in partially delithiated $LiMg_xMn_{1-x}PO_4$ samples, obtained by refinement of the XRD patterns. Since the size of Mg^{2+} (0.86 Å) lies between those of Mn^{2+} (0.98 Å) and Mn^{3+} (0.785 Å), it is understandable that the volume of the lithiated phase decreased while that of the delithiated phase increased with increasing Mg content (Fig. 4c). The presence of unextracted Li in the Mg-substituted phases also tends to increase their cell volumes, leading to smaller mismatches (9.5% for $x = 0$, 4.6% for $x = 0.5$) between the oxidized and reduced phases.

In view of the importance of the phase boundary to the conversion mechanism,[14] it may be that the smaller volume mismatch in the substituted $LiMnPO_4$ facilitates lithium extraction by enhancing the integrity of the phase boundary. The smallest volume mismatch, however was observed for $x = 0.5$, while the delithiated domain size and the best kinetic performance was found at $x = 0.2$. The latter crystals had the largest D_c/D_a ratio among all the Mg-substituted samples, which suggests a role for

morphological factors as well. When 200 mol% of NO_2BF_4 was used, all of the substituted samples were converted to single delithiated phases after 24 h at room temperature (Fig. 5a), with domain sizes increased over those obtained at shorter reaction times (Fig. 5b).

Severe decrepitation was observed in chemically delithiated $LiMnPO_4$ crystals, as shown in the TEM images in Fig. 6. Upon treatment with 50 mol% of NO_2BF_4, the partially delithiated sample, consisting of 93% of $LiMnPO_4$ and 7% of the delithiated Li_yMnPO_4, consisted of ragged skeletal remains of the original crystals surrounded by smaller particles (ca. 25 nm in size) that had broken out of grooves running parallel to the *c*-axis (Fig. 6b). On further delithiation, the initial hexagonal shapes were almost completely destroyed (Fig. 6c). By comparison, on partial delithiation of $LiMg_{0.2}Mn_{0.8}PO_4$, the two-phase sample composed of 70% lithiated and 30% delithiated phosphate showed surface roughening and pitting (Fig. 7b), but the crystals maintained their initial shapes. More extensively delithiated $LiMg_{0.2}Mn_{0.8}PO_4$ crystals displayed grooves, again parallel to the *c*-axis, with more uniform dimensions and spacing (Fig. 7c). Although these crystals had lost much of their mass they retained their original shapes and suffered little reduction in crystallinity. SAED patterns of fresh and delithiated $LiMg_{0.2}Mn_{0.8}PO_4$ crystals are shown in Figure 8. Both lithiated and delithiated phases are present on the partially delithiated crystals (Fig. 8b), which is consistent with the XRD results.

These TEM images of the delithiated crystals provide strong evidence for the course of the phase transition process during delithiation of the Mn phosphates. As is the case in $LiFePO_4$,[14] extraction of Li produces delithiated domains with phase boundaries

in the *bc* plane. These grow in *a* direction, as shown in the schematic in Fig. 9. In $LiMnPO_4$, however, the growth of the newly-formed delithiated domains is limited by the high degree of lattice strain between the phases. The large shrinkage of 7.9% in the *a* direction results in fracturing at or near the phase boundary and ejection of small particles. In contrast to $LiFePO_4$, where the smaller interface strain promotes the growth of the $FePO_4$ domains, [20] the propagation of delithiated ("$MnPO_4$") domains is blocked by fracturing. This helps to explain the poor electrochemical performance of $LiMnPO_4$ with large particle sizes, as decrepitation results in disconnection of the delithiated phase from the conducting matrix. For this reason, good utilization can only be achieved when the initial particle size is quite small.

Mg substitution reduces the volume mismatch between the two end members and thereby reduces the macroscopic strain in $LiMg_xMn_{1-x}PO_4$ crystals. The presence of the larger Mg^{2+} also dilutes the Jahn-Teller ion, Mn^{3+}, and retains Li ions in its vicinity, which may provide a "pillar" effect in the structure. These factors mitigate the local strains between the phases, improving the structural integrity of the crystals and thereby the utilization of capacity.

Fig. 10 compares SEM images of the fully oxidized $Li_xMg_xMn_{1-x}PO_4$ crystals with different levels of substitution. Although the increased physical stability in substituted crystals was evident, the extent of the improvement reached a maximum at 20% Mg substitution, which coincided with the best kinetic performance in the series. These results also point to the importance of the crystal dimension in the *a* crystallographic direction, as it influences the domain size of the nucleating phase and the physical stability of the particles, both of which impact the kinetic performance. Even with Mg

stabilization, the particle size of the phosphate must be small, not only in the *b* dimension, but in *a* as well.

Due to the high electronic resistance in these micron-sized phosphate crystals, the electrochemical behavior of composite electrodes containing $LiMg_xMn_{1-x}PO_4$ (x=0, 0.1 and 0.2) was evaluated using PITT technique. [21,22] The OCV for all three electrodes was 3.200±0.020 V. The incremental capacities ($\Delta Q/\Delta V$) obtained during charging to 4.4 V and then discharging to 3.8 V, with potential steps of 10 mV are compared in Fig. 11. For x = 0, the charging peak was centered at 4.21 V, while the discharge peak appeared at 4.03 V, a difference of 180 mV. Mg substitution slightly increased the separation, to 190 mV and 210 mV for x = 0.1 and 0.2, respectively, with charging peaks at 4.23 V and 4.27 V, and discharging peaks at 4.05 V for both electrodes. The peak shifts may be related to the change in Mn-O bond covalency. Substitution of more electropositive Mg^{2+} for Mn^{2+} decreases M-O covalency and increases the ionicity of Mn metal, which leads to a higher redox potential for Mn^{2+}/Mn^{3+}. Similar effects were previously reported on transition metal substituted $LiM_xMn_{1-x}PO_4$ (M = Fe, Co and Ni). [23,24] Compared to $LiMnPO_4$, the potential of the lower-voltage couple in $LiM_xMn_{1-x}PO_4$ increased while that of the higher-voltage couple decreased.

Among the three electrodes, $LiMg_{0.2}Mn_{0.8}PO_4$ delivered the highest integrated charge capacity of 150 mAh/g, as compared to 100 mAh/g from $LiMnPO_4$ electrode. The charge capacities were higher than the discharge capacities in each case. The low coulombic efficiency may be due to the large particle size. Particle decrepitation and the absence of an intimate carbon coating on the phosphate crystals may have led to

deterioration of the electronic conduction paths during charging for long periods at high potentials, and to lower utilization during the subsequent discharge.

3.3 Improved thermal stability

When heated in an inert atmosphere, chemically delithiated phosphates, $Li_xMg_xMn_{1-x}PO_4$, were found to decompose and release O_2, as evidenced by the XRD studies (Fig. 12). The reaction path, however, is largely influenced by the amount of Mg present. Unsubstituted $LiMnPO_4$ released 0.25 mol of O_2 per mol of the phosphate to form $Mn_2P_2O_7$, starting around 150°C (equation 1). For 50% Mg substitution, the reaction proceeded by an alternate path, releasing 0.125 mol of O_2 per mol of phosphate and forming $Mn_3(PO_4)_2$ (equation 2). For x = 0.1, 0.2, 0.3 and 0.4, both $Mn_2P_2O_7$ and $Mn_3(PO_4)_2$ were detected in the heat-treated samples, the ratio between them decreasing with increasing x.

$$2Li_xMg_xMn_{1-x}PO_4 \rightarrow 2xLiMgPO_4 + (1-x)Mn_2P_2O_7 + 0.5(1-x)O_2 \quad [1]$$

$$3Li_xMg_xMn_{1-x}PO_4 \rightarrow 3xLiMgPO_4 + (1-x)Mn_3(PO_4)_2 + 0.5(1-x)P_2O_5 + 0.75(1-x)O_2 \quad [2]$$

Oxygen released from cathode materials is known to react with the solvents in lithium-ion battery cells. The heat produced can be measured by differential scanning calorimetry (DSC) [4] In the presence of 1M $LiPF_6$ in PC and EC (44:56 by mole ratio), the amount of heat produced decreased monotonically as the Mg content increased from 0 to 0.5, as shown in the DSC profiles of the $Li_xMg_xMn_{1-x}PO_4$ series in Figure 13a. The onset and peak temperatures of the exothermic reaction gradually increased with increasing Mg substitution, while the total heat evolved decreased.

Fig. 13b shows the relationship between the evolved heat and the Mn content in the phosphates. As Mg is electrochemically and chemically inactive, both the theoretical capacity and the released oxygen vary in direct proportion to the Mn content in the phosphates. The Mg-substitution approach, therefore, entails a compromise between rate capability, stability, safety and energy density of the cathode material. We are currently investigating the kinetic and thermal properties of $LiMnPO_4$ in which Mn is substituted by electroactive metals, such as Fe, Co, and Ni.

4. Conclusions

Mg was introduced into the M-site to substitute Mn in $LiMnPO_4$. The presence of Mg^{2+} was found to improve the kinetics and the physical stability of the crystals during chemical and electrochemical delithiation, as well as the thermal stability of the delithiated phase. The best performance was found in the sample with 20% substitution. The positive effect of Mg^{2+} was attributed to the favorable particle morphology, as well as the reduced volume mismatch between the end members. Mg^{2+} also dilutes the concentration of Jahn-Teller active ion, Mn^{3+}, and reduces local stress in the olivine structure, thereby increasing structural stability.

Acknowledgement

The authors acknowledge support of the National Center for Electron Microscopy at Lawrence Berkeley National Laboratory. This work was supported by the Assistant Secretary for Energy Efficiency and Renewable Energy, Office of Vehicle Technologies of the U.S. Department of Energy under Contract No. DE-AC02-05CH11231.

Table 1. Cell parameters of lithiated and delithiated $LiMg_xMn_{1-x}PO_4$ crystals.

$LiMg_xMn_{1-x}PO_4$	Phase	*a* (Å)	*b* (Å)	*c* (Å)	*V* (Å^3)
x=0	Lithiated	10.4474	6.1016	4.7506	302.83
	Delithiated	9.6660	5.9390	4.7785	274.10
x=0.1	Lithiated	10.4189	6.0842	4.7408	300.52
	Delithiated	9.6696	5.9127	4.7787	273.22
x=0.2	Lithiated	10.3888	6.0667	4.7363	298.51
	Delithiated	9.7152	5.9133	4.7774	274.46
x=0.3	Lithiated	10.3613	6.0476	4.7331	296.58
	Delithiated	9.7685	5.9164	4.7756	275.94
x=0.4	Lithiated	10.3258	6.0241	4.728	294.08
	Delithiated	9.8132	5.9183	4.7658	276.74
x=0.5	Lithiated	10.3013	6.0102	4.7221	292.45
	Delithiated	9.911	5.9219	4.7517	278.87

References

[1] A. K. Padhi, K.S. Nanjundaswamy and J.B. Goodenough, *J. Electrochem. Soc.*, 1997, **144**, 1188.

[2] M. Yonemura, A. Yamada, Y. Takei, N. Sonoyama and R. Kanno, *J. Electrochem. Soc.*, 2004, **151**, A1352.

[3] C. Delacourt, L. Laffont, R. Bouchet, C. Wurm, J.-B. Leriche, M. Morcrette, J.-M. Tarascon and C. Masquelier, *J. Electrochem. Soc.*, 2005, **152**, A913.

[4] G. Chen and T. J. Richardson, *J. Power Sources*, 2010, **195**, 1221.

[5] S. P. Ong, A. Jain, G. Hautier, B. Kang and G. Ceder, *Electrochem. Commun.*, 2010, **12**, 427.

[6] C. Delacourt, P. Poizot, M. Morcrette, J.-M. Tarascon and C. Masquelier, *Chem. Mater.*, 2004, **16**, 93.

[7] N.-H. Kwon, T. Drezen, I. Exnar, I. Teerlinck, M. Isono and M. Graetzel, *Electrochem. Solid-State Lett.*, 2006, **9**, A277.

[8] T. R. Kim, D. H. Kim, H. W. Ryu, J. H. Moon, J. H. Lee, S. Boo and J. Kim, *J. Phys. Chem. Solids*, 2007, **68**, 1203.

[9] T. Drezen, N.-H. Kwon, P. Bowen, I. Teerlinck, M. Isono and I. Exnar, *J. Power Sources*, 2007, **174**, 949.

[10] S. K. Martha, B. Markovsky, J. Grinblat, Y. Gofer, O. Haik, E. Zinigrad, D. Aurbach, T. Drezen, D. Wang, G. Deghenghi and I. Exnar, *J. Electrochem. Soc.*, 2009, **156**, A541.

[11] G. Chen, J. D. Wilcox and T. J. Richardson, *Electrochem. Solid-State Lett.*, 2008, **11**, A190.

[12] J. Barker, M. Y. Saidi and T. E. Kelley, US Patent 7,041,239, 2006 (Valence Technology, Inc.)

[13] M. Y. Saidi and H. Huang, US Patent 7,060,238, 2006 (Valence Technology, Inc.)

[14] G. Chen, X. Song and T. J. Richardson, *Electrochem. Solid-State Lett.*, 2006, **9**, A295.

[15] J. Chen, S. Wang and M. S. Whittingham, *J. Power Sources*, 2007, **174**, 442.

[16] J. Chen, M. J. Vacchio, S. Wang, N. Chernova, P. Y. Zavalij and M. S. Whittingham, *Solid State Ionics*, 2008, **178**, 1676.

[17] C. M. Burba and R. Frech, *J. Electrochem. Soc.*, 2004, **151**, A1032.

[18] L. Popović, D. de Wall and J. C. A. Boeyens, *J. Raman Spectrosc.*, 2005, **36**, 2.

[19] G. Chen and T. J. Richardson, *J. Electrochem. Soc.*, 2009, **156**, A756.

[20] C. Delmas, M. Maccario, L. Croguennect, F. L. Cras and F. Weill, *Nat. Mater.*, 2008, **7**, 665.

[21] C. J. Wen, B. A. Boukamp, R. A. Huggins, and W. Weppner, *J. Electrochem. Soc.*, 1979, **126**, 2258.

[22] M. D. Levi and D. Aurbach, *J. Solid State Electrochem.*, 2007, **11**, 1031.

[23] G. Kobayashi, A. Yamada, S.-I. Nishimura, R. Kanno, Y. Kobayashi, S. Seki, Y. Ohno and H. Miyashiro, *J. Power Sources*, 2009, **189**, 397.

[24] H. Gwon, D.-H. Seo, S.-W. Kim, J. Kim and K. Kang, *Adv. Funct. Mater.*, 2009, **19**, 3285.

Figure captions

1. a) XRD patterns and b) lattice parameters of $LiMg_xMn_{1-x}PO_4$ crystals.
2. FTIR spectra of $LiMg_xMn_{1-x}PO_4$ crystals.
3. a) SEM images and b) D_c/D_a ratios of $LiMg_xMn_{1-x}PO_4$ crystals.
4. $LiMg_xMn_{1-x}PO_4$ crystals treated with 50 mol% of NO_2BF_4: a) XRD patterns, b) percentage and domain size of the delithiated phase and c) cell volumes of the lithiated and the delithiated phases.
5. a) XRD patterns of $LiMg_xMn_{1-x}PO_4$ crystals treated with 200 mol% of NO_2BF_4 and b) comparison of delithiated domain sizes in crystals treated with 50 and 200 mol% of NO_2BF_4.
6. TEM images of $LiMnPO_4$ crystals: a) fresh, b) treated with 50 mol% of NO_2BF_4 and c) treated with 200 mol% of NO_2BF_4.
7. TEM images of $LiMg_{0.2}Mn_{0.8}PO_4$ crystals: a) fresh, b) treated with 50 mol% of NO_2BF_4 and c) treated with 200 mol% of NO_2BF_4.
8. Electron diffraction patterns of $LiMg_{0.2}Mn_{0.8}PO_4$ crystals: a) fresh, b) treated with 50 mol% of NO_2BF_4 and c) treated with 200 mol% of NO_2BF_4.
9. Schematic diagram of the phase transformation mechanism during the delithiation of Mn phosphates.
10. SEM images of $LiMg_xMn_{1-x}PO_4$ crystals treated with 200 mol% of NO_2BF_4.
11. PITT data for $LiMg_xMn_{1-x}PO_4$ (x = 0, 0.1 and 0.2) composite electrodes.
12. XRD patterns of heat-treated $Li_xMg_xMn_{1-x}PO_4$ (x = 0, 0.2 and 0.5) crystals.
13. a) DSC profiles of the $Li_xMg_xMn_{1-x}PO_4$ crystals in the presence of electrolyte and b) the relationship between the heat evolved and the Mn content in the phosphates.

Figure 1

a)

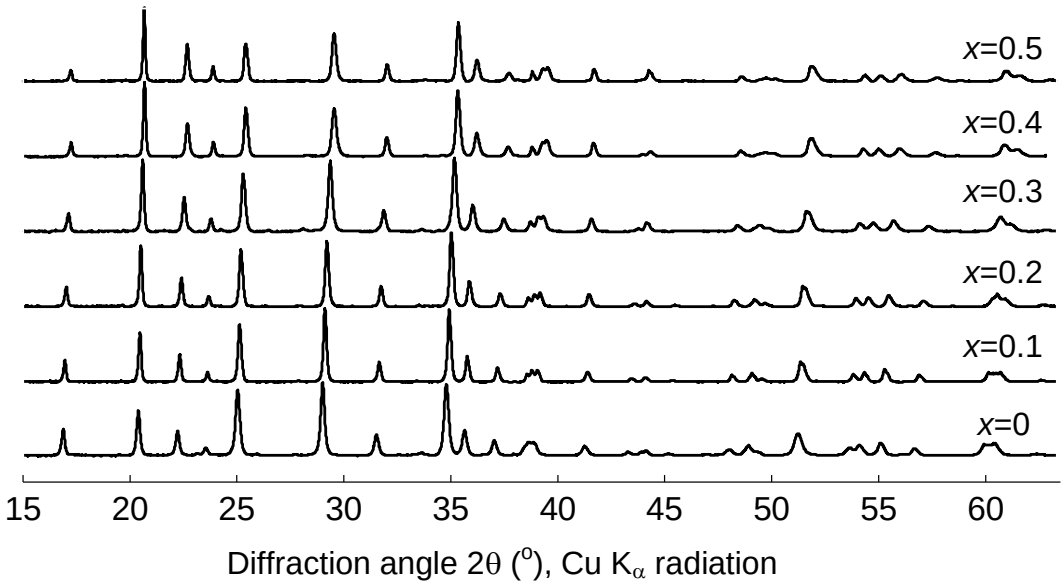
x=0.5
x=0.4
x=0.3
x=0.2
x=0.1
x=0
15 20 25 30 35 40 45 50 55 60
Diffraction angle 2θ (°), Cu Kα radiation

b)

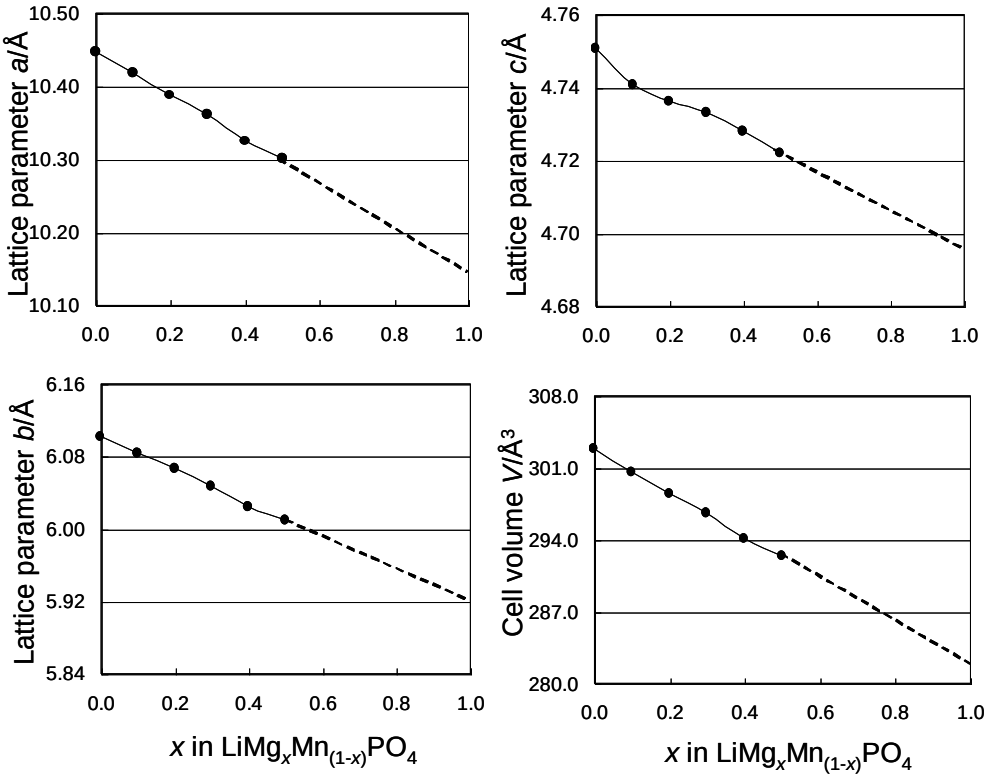
Lattice parameter a/Å
10.50 10.40 10.30 10.20 10.10
Lattice parameter c/Å
4.76 4.74 4.72 4.70 4.68
Lattice parameter b/Å
6.16 6.08 6.00 5.92 5.84
Cell volume V/Å3
308.0 301.0 294.0 287.0 280.0
0.0 0.2 0.4 0.6 0.8 1.0
x in LiMgxMn(1-x)PO4

Figure 2

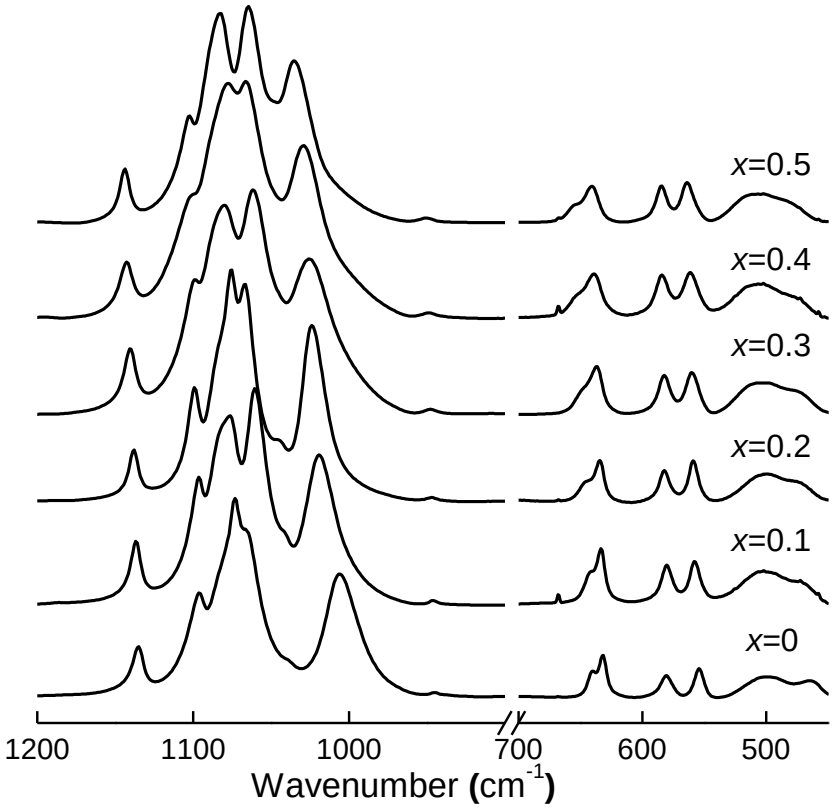
x=0.5
x=0.4
x=0.3
x=0.2
x=0.1
x=0
1200
1100
1000
700
600
500
Wavenumber (cm-1)

Figure 3

a)

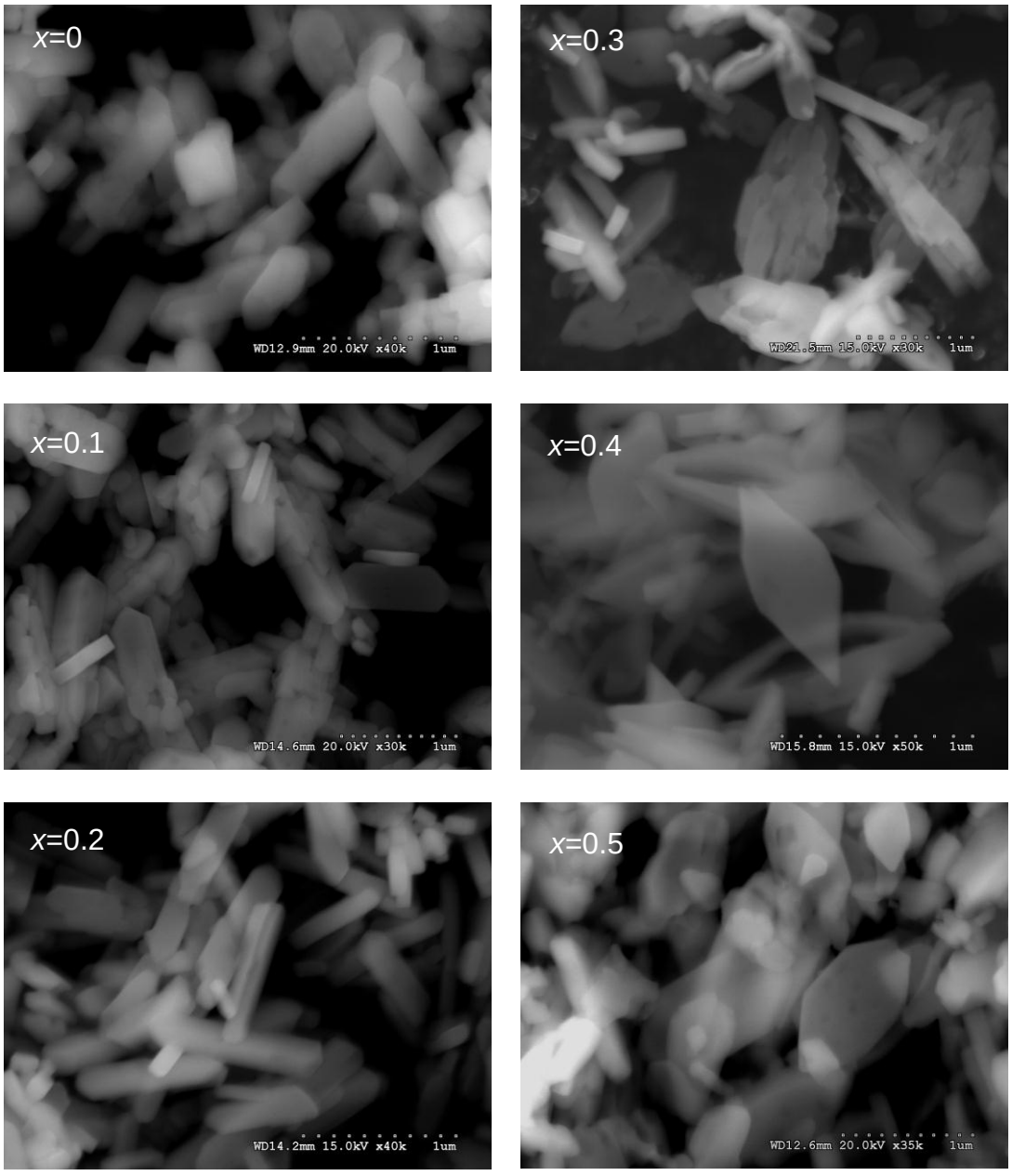
x=0
WD12.9mm 20.0kV x40k 1um
x=0.3
WD21.5mm 15.0kV x30k 1um
x=0.1
WD14.6mm 20.0kV x30k 1um
x=0.4
WD15.8mm 15.0kV x50k 1um
x=0.2
WD14.2mm 15.0kV x40k 1um
x=0.5
WD12.6mm 20.0kV x35k 1um

b)

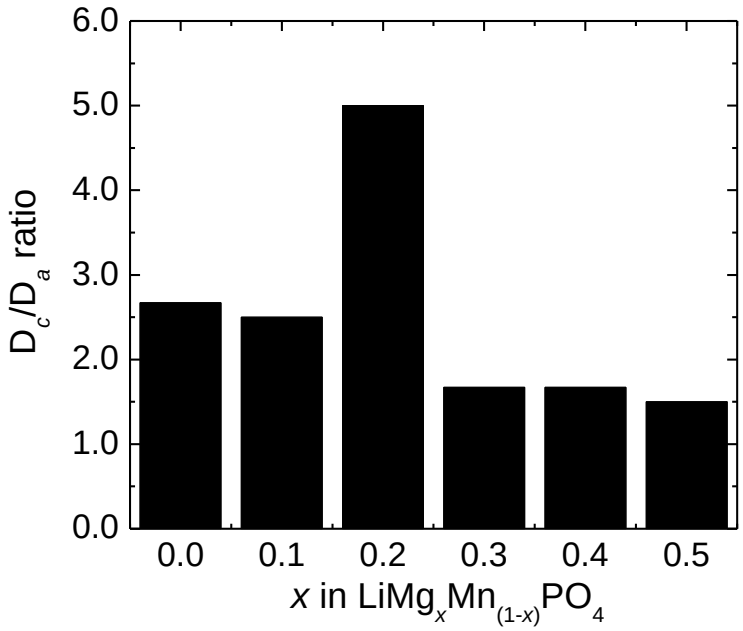
6.0
5.0
4.0
3.0
2.0
1.0
0.0
D$_c$/D$_a$ ratio
0.0
0.1
0.2
0.3
0.4
0.5
x in LiMg$_x$Mn$_{(1-x)}$PO$_4$

Figure 4

a)

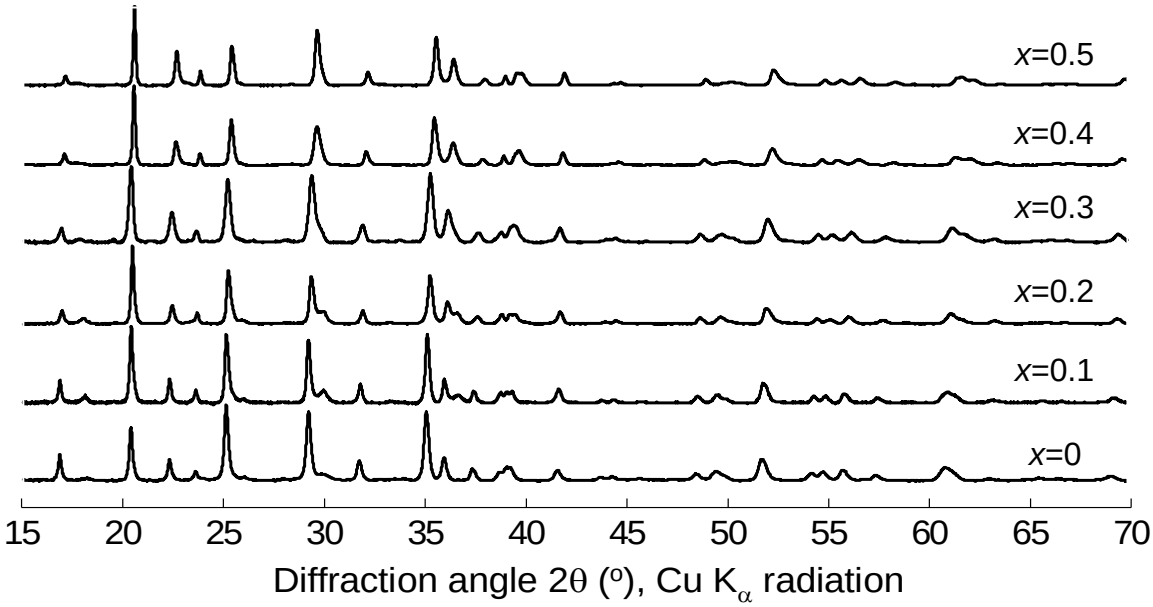
x=0.5
x=0.4
x=0.3
x=0.2
x=0.1
x=0
15 20 25 30 35 40 45 50 55 60 65 70
Diffraction angle 2θ (º), Cu Kα radiation

b)

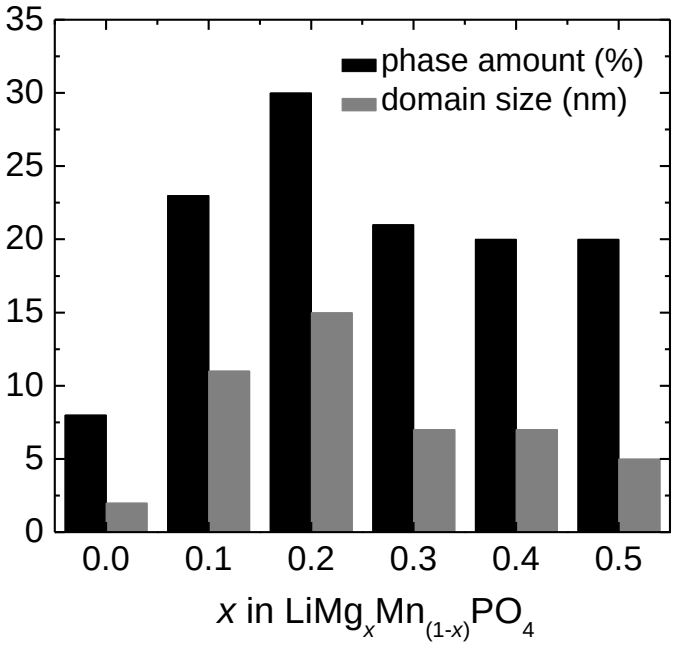
phase amount (%)
domain size (nm)
0 5 10 15 20 25 30 35
0.0 0.1 0.2 0.3 0.4 0.5
x in LiMgxMn(1-x)PO4

c)

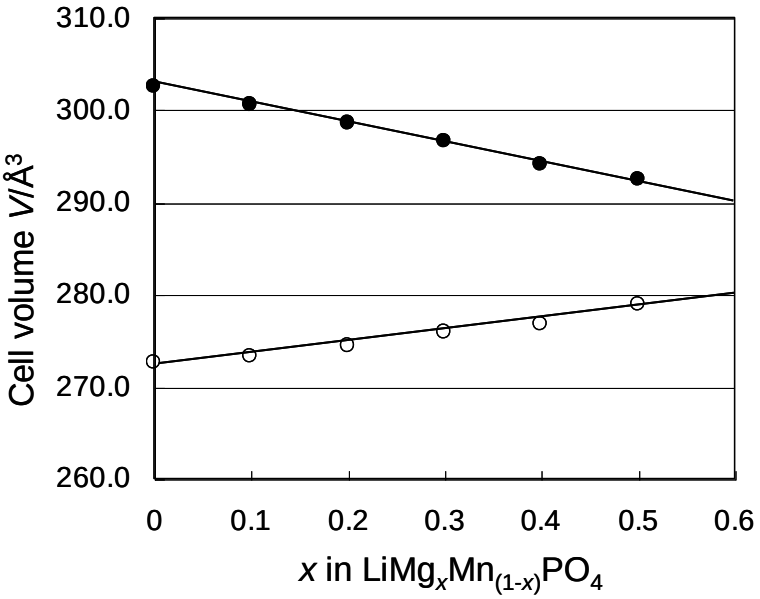
310.0
300.0
290.0
280.0
270.0
260.0
Cell volume V/Å3
0
0.1
0.2
0.3
0.4
0.5
0.6
x in LiMgxMn(1-x)PO4

Figure 5

a)

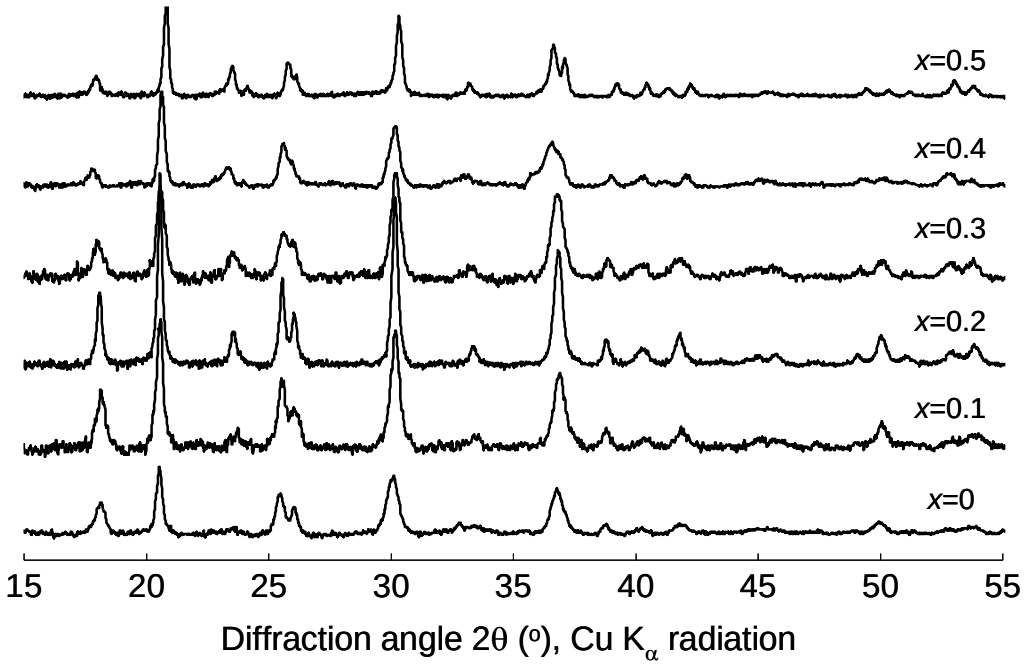
x=0.5
x=0.4
x=0.3
x=0.2
x=0.1
x=0
15
20
25
30
35
40
45
50
55
Diffraction angle 2θ (º), Cu Kα radiation

b)

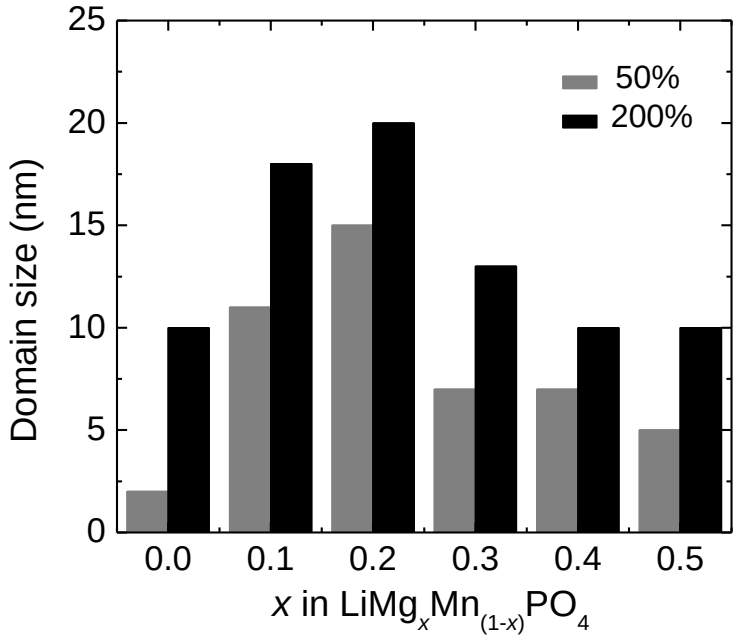
25
20
15
10
5
0
50%
200%
Domain size (nm)
0.0
0.1
0.2
0.3
0.4
0.5
x in LiMgxMn(1-x)PO4

Figure 6

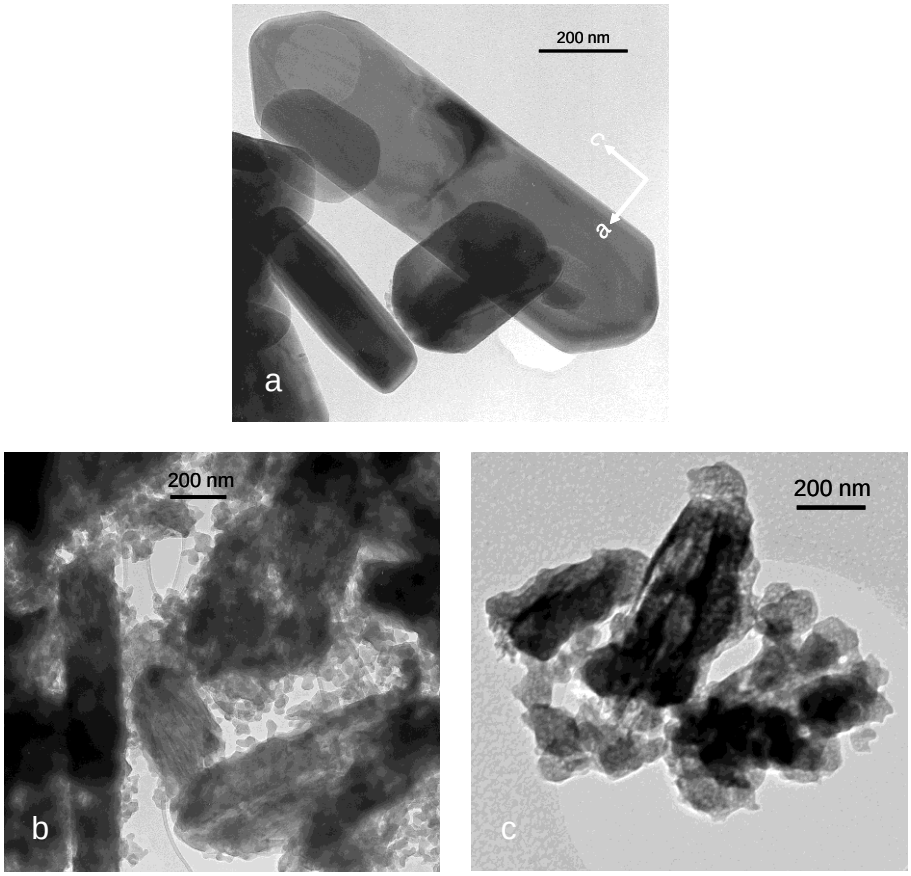

Figure 7

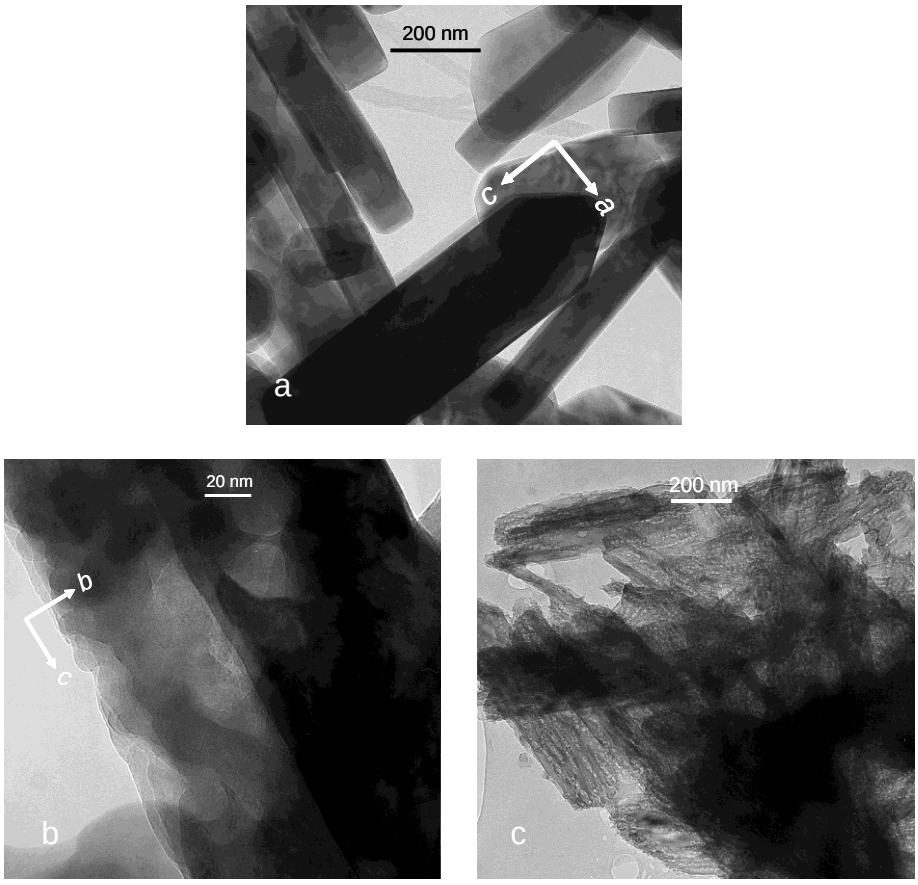

Figure 8

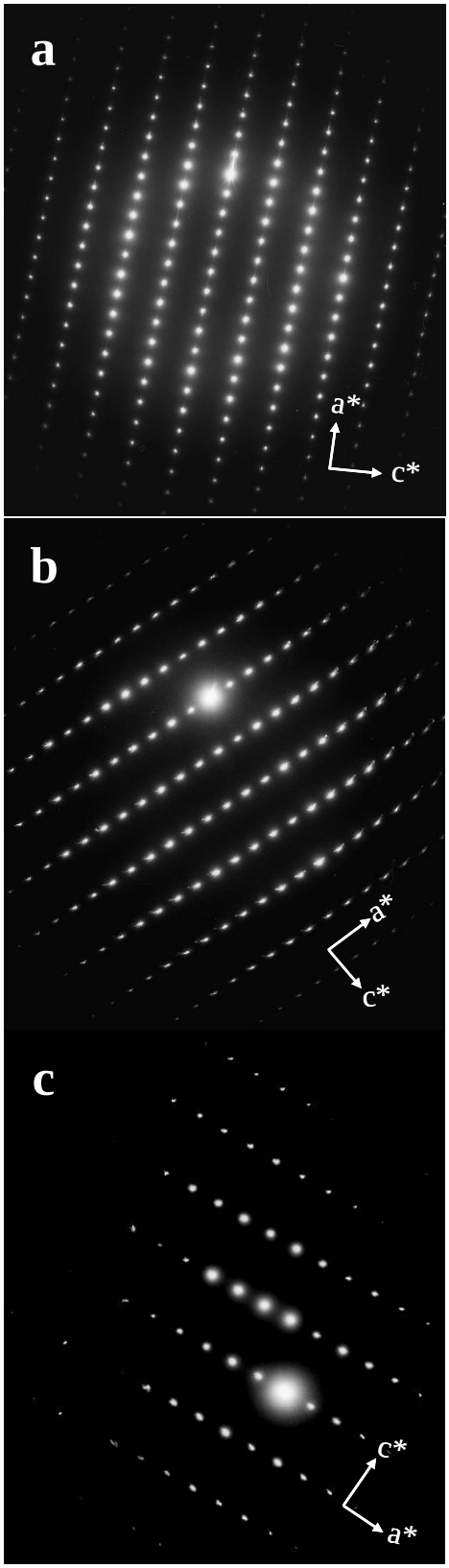

Figure 9

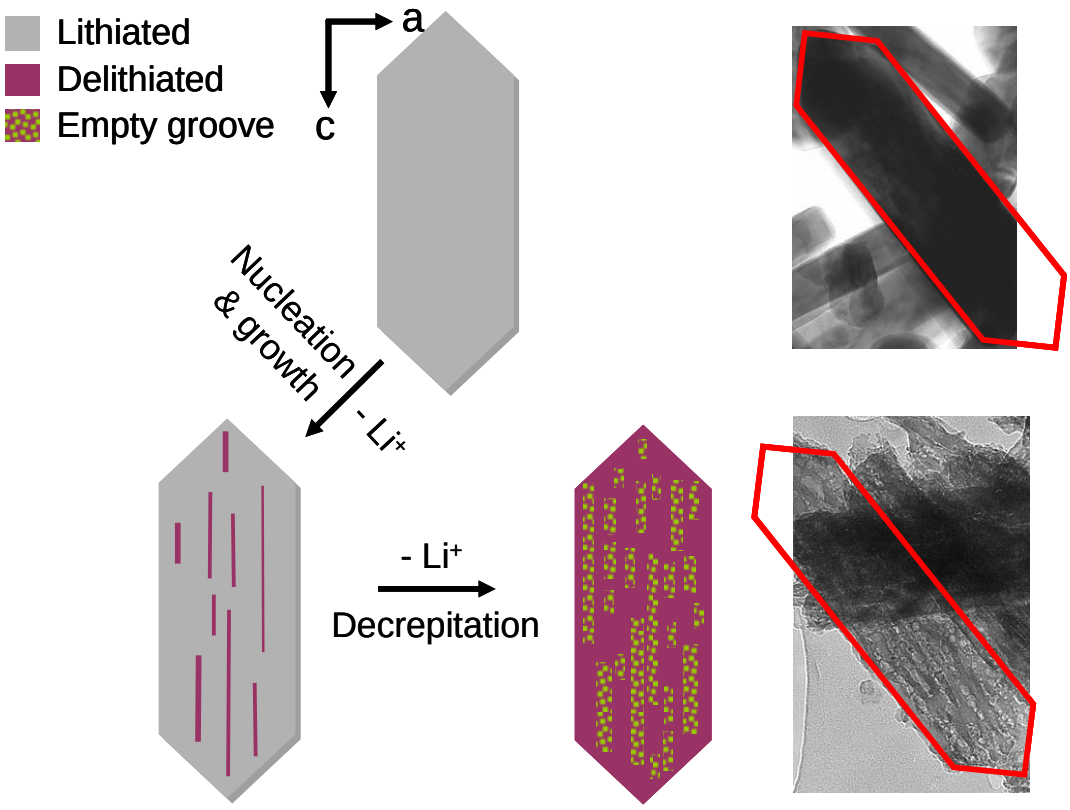
Lithiated
Delithiated
Empty groove
a
c
Nucleation & growth
- Li+
- Li+
Decrepitation

Figure 10

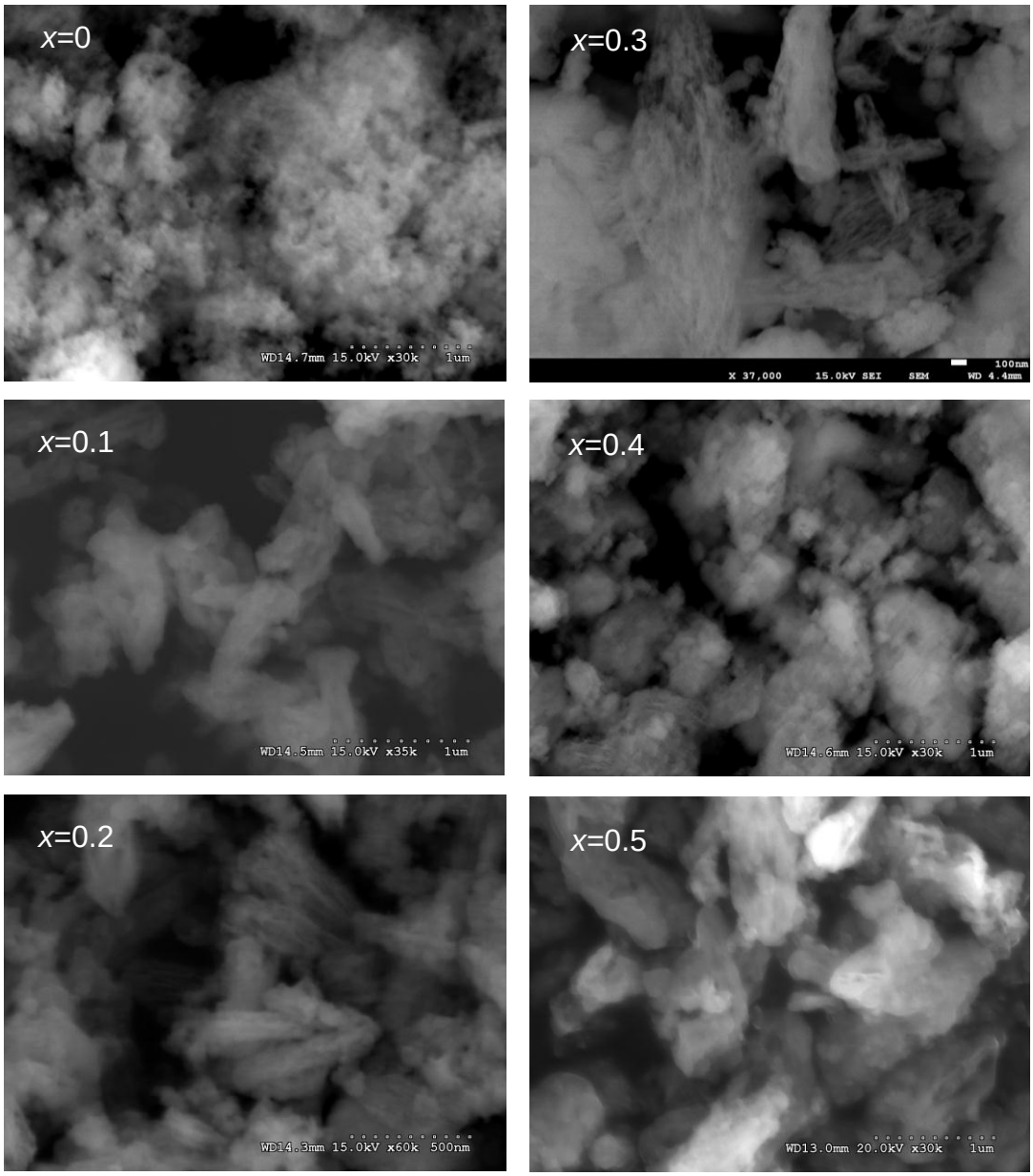
x=0
WD14.7mm 15.0kV x30k 1um
x=0.3
X 37,000 15.0kV SEI SEM WD 4.4mm 100nm
x=0.1
WD14.5mm 15.0kV x35k 1um
x=0.4
WD14.6mm 15.0kV x30k 1um
x=0.2
WD14.3mm 15.0kV x60k 500nm
x=0.5
WD13.0mm 20.0kV x30k 1um

Figure 11

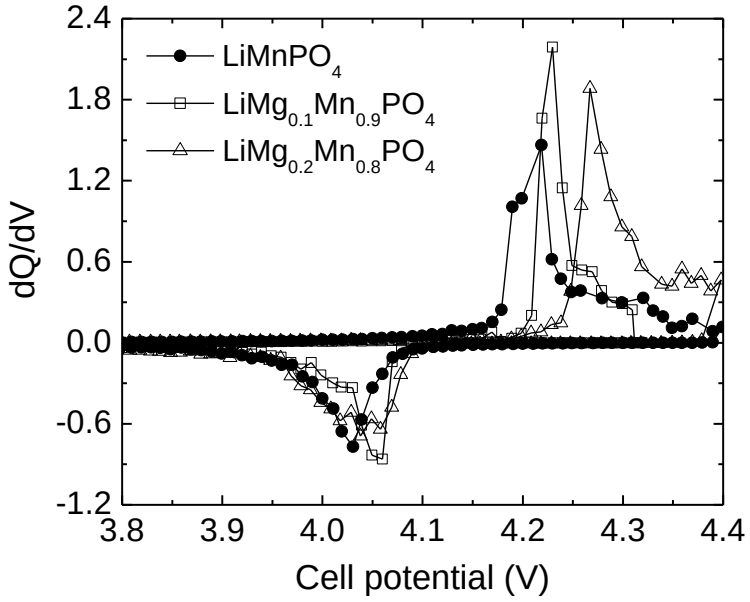
LiMnPO4
LiMg0.1Mn0.9PO4
LiMg0.2Mn0.8PO4
dQ/dV
Cell potential (V)
2.4
1.8
1.2
0.6
0.0
-0.6
-1.2
3.8
3.9
4.0
4.1
4.2
4.3
4.4

Figure 12

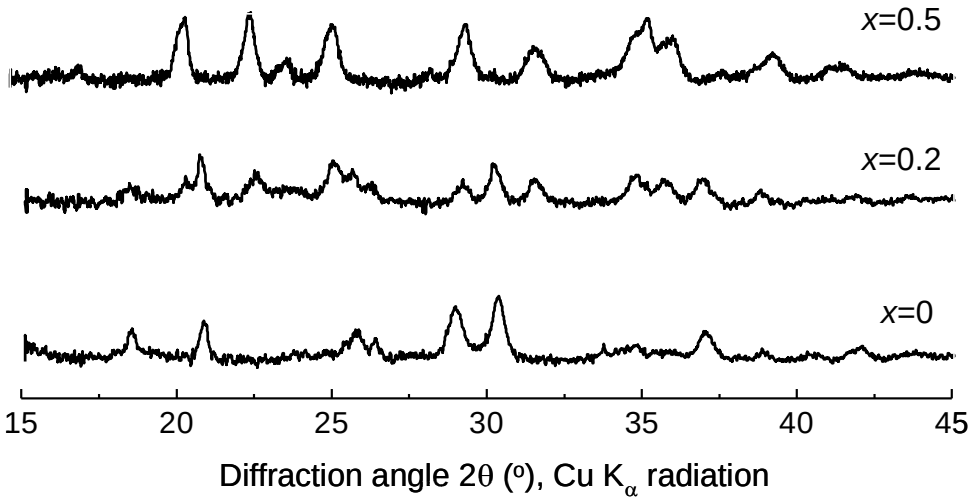
x=0.5
x=0.2
x=0
15
20
25
30
35
40
45
Diffraction angle 2θ (º), Cu Kα radiation

Figure 13

a)

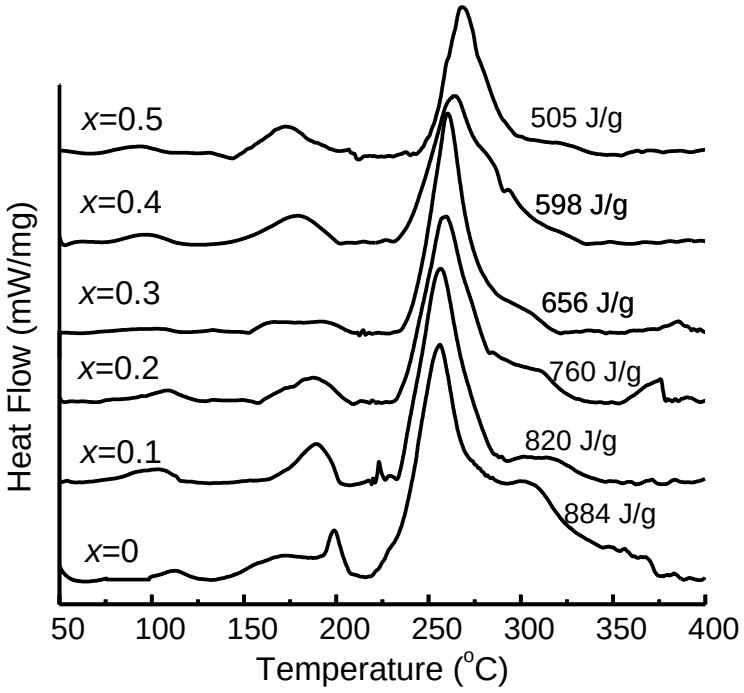
x=0.5
505 J/g
x=0.4
598 J/g
x=0.3
656 J/g
x=0.2
760 J/g
x=0.1
820 J/g
884 J/g
x=0
Heat Flow (mW/mg)
50
100
150
200
250
300
350
400
Temperature (°C)

b)

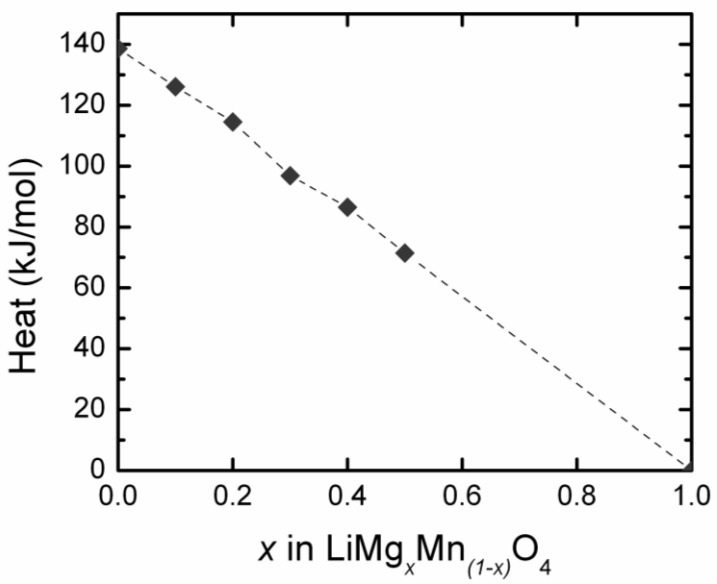
Heat (kJ/mol)
0
20
40
60
80
100
120
140
0.0
0.2
0.4
0.6
0.8
1.0
x in LiMgxMn(1-x)O4

DISCLAIMER